Impedance Adaptive Dual-Mode Control of Grid-Connected Inverters With Large Fluctuation of SCR and Its Stability Analysis Based on D-Partition Method

Ming Li, *Member, IEEE*, Xing Zhang, *Senior Member, IEEE*, Zixuan Guo, *Student Member, IEEE*, Hailong Pan, Mingyao Ma, *Member, IEEE*, and Wei Zhao

***Abstract*—The stable operation of grid-connected inverters (GCIs) with traditional current source mode (CSM) control is affected by the large fluctuations of short-circuit ratio (SCR) under weak grids. Improved CSM control enhances the stability of GCIs under weak grids but remains unstable for very weak grids, while the stability of GCIs with voltage source mode (VSM) is just the opposite. Therefore, previous research works have proposed the impedance adaptive dual-mode control strategy: when the SCR is large, the GCI is controlled by CSM, and when the SCR is small, it is controlled by VSM. However, the existing literature still lacks the analysis of the parameter stability region and mode switching boundary of GCI in different modes. Therefore, based on the D-partition method, this article derives the parameter stability region of GCI in different modes under the constraints of multiple performance indexes such as phase and gain margin, current-loop bandwidth and phase-locked loop bandwidth, and the switching boundaries of CSM and VSM are also proposed. Finally, based on the grid impedance identification algorithm, the impedance adaptive dual-mode control is realized, which effectively improves the stability of GCI when SCR fluctuates greatly, and the experimental results verify the correctness of the above analysis.**

***Index Terms*—Dual mode, grid-connected inverter, grid impedance, short-circuit ratio (SCR), stability analysis, weak grid.**

I. Introduction

With the increasing penetration and the decentralized location of distributed power generation system (DPGS), long-distance transmission lines and multiple transformers are used to connect the DPGS to the public grid. As a result, the public grid presents weak grid characteristics with low short-circuit ratio (SCR) (the ratio of short-circuit level to the rated capacity of the system) due to the nonignorance of grid impedance [1]–[3]. In addition, the volatility and intermittency of new energy generation will also lead to significant SCR fluctuations, which poses a serious challenge to the stable and efficient operation of grid-connected inverters (GCIs).

In order to achieve stable DPGS, the control design of GCIs should be adequately addressed. There are two basic control modes for GCIs: current source mode (CSM) and voltage source mode (VSM) [4]–[6]. For CSM-controlled GCI, it is based on the typical vector control with phase-locked loop (PLL) synchronization technique [7]. The CSM-controlled GCI is widely used because of its good dynamic response and disturbance rejection capability [8]. However, it has been reported that the dynamics of the CSM-controlled GCI becomes more complicated when connected to a weak grid and undesirable oscillations or stability issues arise [1], [9], [10]. Some related stability control strategies have been published, such as adjusting PI controller parameters or structure [11], adding active damping control [1], [4], modifying grid voltage feedforward control [12], reducing the PLL bandwidth [13], etc., these strategies can improve the stability of CSM-controlled GCI in weak grids to some extent. However, by constructing a static power transfer model of the CSM-controlled GCI in the dq-axis coordinate system, Li *et al.* [6] found that the output active power of the CSM-controlled GCI will no longer be monotonic with the grid current command value if the grid impedance is very large. Therefore, in order to ensure the stability and sufficient dynamic performance of the GCI when the grid impedance is very high, an alternative control mode is required.

As another control mode, a VSM-controlled GCI [6], [14]–[16] has been proposed. The GCI in this mode controls the output power of the GCI directly by adjusting the amplitude and phase of the output voltage without using a PLL system. Its synchronization process with grid frequency and phase is achieved by a droop-controlled power self-synchronization loop. For example, Zhang *et al.* [14] proposed the so-called power synchronization

Manuscript received January 13, 2021; revised April 25, 2021; accepted May 28, 2021. Date of publication June 7, 2021; date of current version August 16, 2021. This work was supported in part by the National Natural Science Foundation of China-State Grid Joint Fund for Smart Grid under Grant U1766207, and in part by the National Natural Science Foundation of China under Grant 51677049. Recommended for publication by Associate Editor X. Wang. *(Corresponding author: Ming Li.)*

Ming Li, Xing Zhang, Zixuan Guo, Hailong Pan, and Mingyao Ma are with the National and Local Joint Engineering Laboratory for Renewable Energy Access to Grid Technology, School of Electrical Engineering and Automation, Hefei University of Technology, Hefei 230009, China (e-mail: jhuumi@163.com; honglf@ustc.edu.cn; g_zixuan@126.com; 2730738788@qq.com; miyama@hfut.edu.cn).

Wei Zhao is with the Sungrow Power Supply Co., Ltd., Hefei 230088, China (e-mail: zhaow@sungrowpower.com).

Color versions of one or more figures in this article are available at https://doi.org/10.1109/TPEL.2021.3087028.

Digital Object Identifier 10.1109/TPEL.2021.3087028

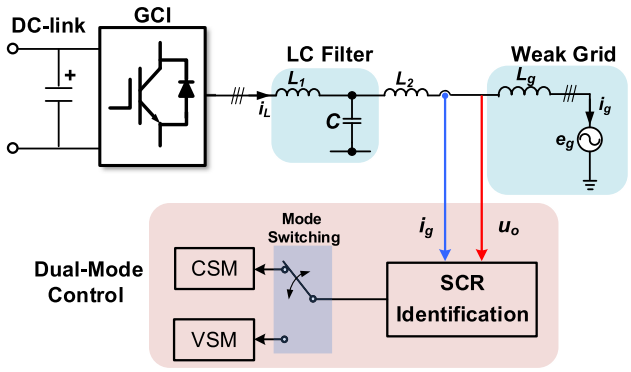

Fig. 1. Schematic diagram of impedance adaptive dual-mode control under large SCR fluctuations.

control that enables the GCI output voltage to be synchronized with grid phase, and the method has been shown to be a superior solution for high-voltage dc (HVdc) transmission connected to very weak ac systems. Yuan *et al.* [15] investigated the dc-side voltage stabilization control strategy of a permanent magnet wind turbine with full-power VSM-controlled GCI under weak grid conditions. Wu *et al.* [16] studied the VSM-controlled GCI based on virtual synchronous generator control and pointed out that the VSM-controlled GCI exhibited better stability compared with the CSM-controlled GCI when the grid impedance was large. Moreover, Li *et al.* [6] found that if the grid impedance is small, the damping ratio of the droop-controlled power self-synchronization loop will decrease, which will lead to its output active power being prone to oscillation and thus no longer stable.

In summary, the CSM-controlled GCI and the VSM-controlled GCI have exactly opposite stability characteristics under different grid strengths. Based on this conclusion, Li *et al.* [6] proposed a dual-mode control strategy: in the strong grid, the GCI operates in the CSM, while in the weak grid, it operates in the VSM. The schematic diagram of the impedance adaptive dual-mode control strategy is given in Fig. 1. The strategy uses a grid impedance identification algorithm to obtain SCR, and then the GCI adaptively determines whether to operate in CSM or VSM to improve the system stability under large fluctuations in SCR. It can be seen that the key of this control strategy lies in the switching boundary of CSM and VSM. However, [6] only qualitatively considered the switching boundary of the two grid-connected modes as SCR=2 according to IEEE Standard 1204-1997, and did not quantitatively analyze the switching boundary of the two grid-connected modes, nor does it propose a method to achieve perturbation-free switching between the two grid-connected modes.

Therefore, the contributions of this article are as follows.

1) A stability control method based on grid impedance adaptive dual-mode control of GCI is proposed. The method effectively improves the stability of GCI under large SCR fluctuations by perturbation-free adaptive switching of GCI between CSM control and VSM control.
2) The mode switching boundaries of the proposed dual-mode control method are obtained quantitatively. In this article, the D-partition method [17]–[22] is used to obtain the parameter stability region of CSM-controlled GCI and VSM-controlled GCI under the constraints of multiple performance indexes such as gain margin, phase margin and control bandwidth, respectively, so as to determine the stability boundaries between two modes. Compared with the traditional Routh criterion [23], Bode plot [24], Nyquist plot [25], and other methods, the analysis results do not require repeated trial and error, and the parameter stability region under the constraints of multiple performance indexes can be obtained.

The rest of this article is organized as follows. In Sections II and III, the CSM-controlled GCI and the VSM-controlled GCI are modeled and their stability are analyzed based on the D-partition method, respectively, and the switching boundaries between the two modes under constraints of multiple performance index are given. Section IV introduces the grid impedance identification method and the principle of proposed dual-mode seamless switching algorithm. The validity of the above analysis is verified by the 100-kW experimental platform in Section V. Finally, Section VI gives the conclusion of this article.

II. Modeling and Stability Analysis of CSM-Controlled GCI Based on D-Partition Method

A. Modeling of CSM-Controlled GCI

To obtain the small-signal model of the GCI, Sun *et al.* [26], [27] proposed the harmonic linearization method to establish its positive- and negative-sequence impedance models, and the stability of the typical GCI connected to the grid was studied by the impedance-based stability criterion.

Fig. 2 shows the main circuit of the GCI in this article. Where $V_{\rm dc}$ stands for the dc voltage, L_1, $C_{\rm f}$ constitute the *LC* filter, L_1 is the inverter-side inductance, and $C_{\rm f}$ is the filter capacitance. $R_{\rm d}$ is the passive damping resistance. L_2 is the equivalent small inductance, which represents the line impedance of the ac cable connecting the inverter to the point of common coupling (PCC). $L_{\rm g}$ represents the grid impedance. $u_{\rm oabc}$ is the voltage of PCC. $u_{\rm Cabc}$ is the total voltage on $C_{\rm f}$ and $R_{\rm d}$. $i_{\rm gabc}$ and $i_{\rm Labc}$ are the grid current and inverter-side current, respectively.

The control structure and control block diagram of the CSM-controlled GCI are shown in Figs. 3 and 4, respectively. In Fig. 3, $i_{\rm Ldref}$ and $i_{\rm Lqref}$ are the d-axis and q-axis components of the reference current $i_{\rm Lref}$ in the current loop, $\theta_{\rm CSM}$ is the phase obtained by the PLL according to $u_{\rm oabc}$. The GCI will be controlled with the characteristics of a current source, as it is phase-synchronized to the grid voltage based on the PLL, and then adjusts the grid current command value to regulate the power injected into the grid. From Fig. 4, the expression of transfer function of the output current is

$$i_{\rm g}(s) = G_{\rm cl\_CSM}(s) i_{\rm gref}(s) - u_{\rm o}(s)/Z_{\rm o\_CSM}(s) \qquad (1)$$

where $G_{\rm cl\_CSM}(s)$ and $Z_{\rm o\_CSM}(s)$ are the closed-loop transfer function and the output impedance of the CSM-controlled GCI, respectively. According to the harmonic linearization method, $G_{\rm cl\_CSM}(s)$ can be divided into positive-sequence closed-loop transfer function $G_{\rm cl\_CSM\_p}(s)$ and negative-sequence closed-loop transfer function $G_{\rm cl\_CSM\_n}(s)$, $Z_{\rm o\_CSM}(s)$ can be divided

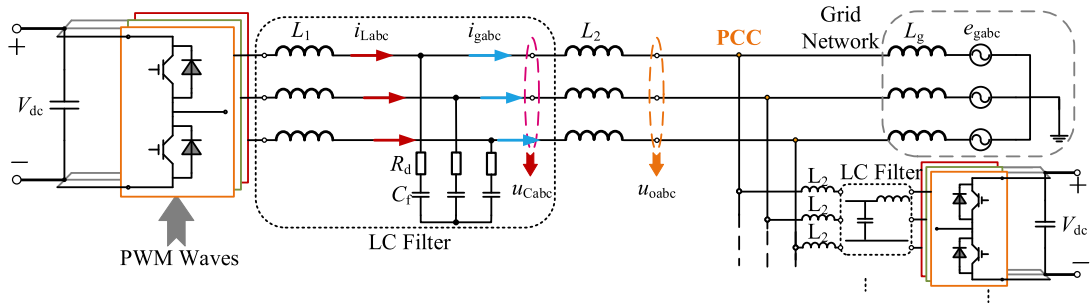

Fig. 2. Main circuit of the GCI.

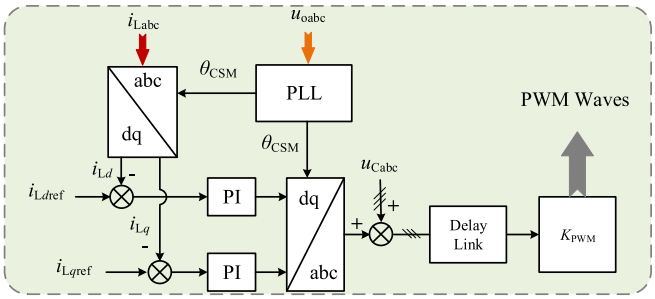

Fig. 3. Control structure of the CSM-controlled GCI.

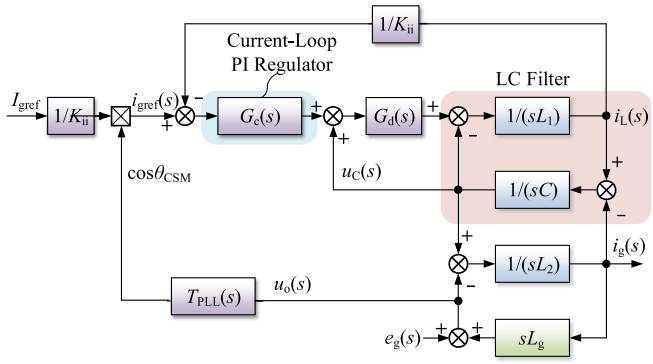

Fig. 4. Control block diagram of the CSM-controlled GCI.

into positive-sequence impedance $Z_{o\_CSM\_p}(s)$ and negative-sequence impedance $Z_{o\_CSM\_n}(s)$ [13]. Their expressions are

$$G_{cl\_CSM\_p}(s) = G_c(s-j\omega_0)\,G_d(s)/K_{ii} \Big/ \begin{Bmatrix} s^3L_1L_2C + s^2L_2C/K_{ii}G_c(s-j\omega_0) \\ \cdot G_d(s) + s(L_1+L_2) \\ +G_c(s-j\omega_0)\,G_d(s)/K_{ii} \end{Bmatrix} \tag{2}$$

$$G_{cl\_CSM\_n}(s) = G_c(s+j\omega_0)\,G_d(s)/K_{ii} \Big/ \begin{Bmatrix} s^3L_1L_2C + s^2L_2C/K_{ii}G_c(s+j\omega_0) \\ \cdot G_d(s) + s(L_1+L_2) \\ +G_c(s+j\omega_0)\,G_d(s)/K_{ii} \end{Bmatrix} \tag{3}$$

$$Z_{o\_CSM\_p}(s) = sL_2 + \frac{sL_1 + G_c(s-j\omega_0)\,G_d(s)/K_{ii}}{\begin{Bmatrix} 1+s^2L_1C + sCG_c(s-j\omega_0)\,G_d(s)/K_{ii} \\ -G_d(s) - T_{PLL}(s-j\omega_0)/[1+T_{PLL}(s-j\omega_0)] \\ \cdot \begin{bmatrix} G_c(s-j\omega_0)\,I_1/V_1 + (V_1 + jL_1I_1\omega_0) \\ \cdot e^{j\phi_{c1}}/(2V_1) \end{bmatrix} \end{Bmatrix}} \tag{4}$$

$$Z_{o\_CSM\_n}(s) = sL_2 + \frac{sL_1 + G_c(s+j\omega_0)\,G_d(s)/K_{ii}}{\begin{Bmatrix} 1+s^2L_1C + sCG_c(s+j\omega_0)\,G_d(s)/K_{ii} \\ -G_d(s) - T_{PLL}(s+j\omega_0)/[1+T_{PLL}(s+j\omega_0)] \\ \cdot \begin{bmatrix} G_c(s+j\omega_0)\,I_1/V_1 + (V_1 + jL_1I_1\omega_0) \\ \cdot e^{-j\phi_{c1}}/(2V_1) \end{bmatrix} \end{Bmatrix}}. \tag{5}$$

In (2)–(5), K_{ii} is the sampling coefficient of the current sensor. $C = sC_f/(sC_fR_d + 1)$ represents the equivalent capacitance of R_d and C_f in series. $G_c(s)$=$K_{p\_CSM} + K_{i\_CSM}/s$ represents the PI current regulator. $G_d(s)$=$e^{-sT_s}(1 - e^{-sT_s})/(sT_s)$ presents digital control delays [28], where T_s is the sampling period of inverter. V_1 and I_1 are the amplitude of grid voltage and grid current, respectively. ω_0 is the rated fundamental angular frequency. ϕ_{c1} is the angle between dq-axis modulation voltage. $T_{PLL}(s) = \sqrt{\frac{3}{2}}V_1[K_{pPLL} + K_{iPLL}/s]/s$ stands for the transfer function of three-phase synchronous reference frame PLL (SRF-PLL), where K_{pPLL} and K_{iPLL} represent the PI coefficients of the PLL regulator, respectively.

The main parameters of the GCI are shown in Table I.

B. Principle of D-Partition Method

The D-partition (or D-decomposition) method was originally proposed by Lanzkron and Higgins in 1959 [17]. Shenton and Shafiei [19], [20] developed the D-partition method in 1994 based on the open-loop frequency response, called the open-loop D-partition method. As a frequency domain method, the D-partition method can easily depict the stability boundaries of the controller parameters without considering the form of the characteristic polynomial, and thus, can deal with stable and unstable systems with time delays, which it is difficult to discuss the roots of the characteristic equations. Also, the D-partition method can deal with stable regions with certain

TABLE I
MAIN PARAMETERS OF GCI

Symbol	Name	Value
P_{n}	rated capacity	100 kW
E_{n}	rated grid voltage	220 V
ω_0	rated fundamental angular frequency	100π rad/s
f_{sw}	switching frequency	16 kHz
f_{s}	sampling frequency	16 kHz
L_1	inverter-side inductance	0.9 mH
C_{f}	filter capacitance	20 μF
L_2	grid-side inductance of the AC cable	50 μH
R_{d}	passive damping resistance	0.6 Ω
K_{ii}	sampling coefficient of the current sensor	29 p.u.
K_{vv}	sampling coefficient of the voltage sensor	400 p.u.
K_{c}	gain of inner current-loop P regulator	200 Ω
K_{pPLL}	integration coefficient of PI regulator of SRF-PLL	0.0012 (rad/s) /V
K_{iPLL}	proportion coefficient of PI regulator of SRF-PLL	0.0007 (rad/s) /V
V_1	amplitude of rated grid voltage	311 V
I_1	amplitude of rated grid current	212 A

relative stability margins and be used to analyze the stability of control systems [21], [22].

A typical closed-loop characteristic polynomial of the control system can be expressed as follows [18]:

$$p\left(s;k\right)=a_0(k)+a_1(k)s+\cdots+a_i(k)s^i+\cdots+a_n(k)s^n. \tag{6}$$

Equation (6) is an n-dimensional characteristic polynomial with s as the variable, the coefficient $a_i(k)$ is a r-dimensional parameter function of $k=\{k_1,k_2,\ldots,k_r\}$, and the parameter domain is denoted as $\mathbf{K}$. Since the roots of the polynomial are continuous function of the coefficients [18], the corresponding relationship between the roots of the characteristic polynomial and the parameter domain $\mathbf{K}$ can be established.

The D-partition boundary is composed of points $k\in\mathbf{K}$, and these points satisfy the characteristic polynomial and have at least one root on the imaginary axis of the s-plane. Therefore, the D-partition boundary can be composed of $p(0;k)=0$, $p(\infty;k)=0$, $p(\pm j\omega;k)=0$ [18]

$$\begin{cases} D_0=\{k\in\mathbf{K}:p\left(0;k\right)=0\} \\ D_\infty=\{k\in\mathbf{K}:p\left(\infty;k\right)=0\} \\ D_\omega=\{k\in\mathbf{K}:p\left(\pm j\omega;k\right)=0,\forall\omega\in(0,\infty)\}. \end{cases} \tag{7}$$

Based on (7), D_0, D_∞ can be obtained as $a_0(k)=0, a_n(k)=0$, and D_ω can be equivalent to

$$\begin{cases} a_0(k)-a_2(k)\omega^2+a_4(k)\omega^4-\cdots=0 \\ a_1(k)-a_3(k)\omega^2+a_5(k)\omega^4-\cdots=0. \end{cases} \tag{8}$$

For example, for a unit negative feedback system as shown in Fig. 5(a), if $G_{\mathrm{o}}(s)|_{s=j\omega}=[K_{\mathrm{p}}+K_{\mathrm{i}}/(j\omega)][a(\omega)+jb(\omega)]$, then (8) is derived as

$$\begin{cases} 1+K_{\mathrm{p}}a\left(\omega\right)+\frac{K_{\mathrm{i}}}{\omega}b\left(\omega\right)=0 \\ K_{\mathrm{p}}b\left(\omega\right)-\frac{K_{\mathrm{i}}}{\omega}a\left(\omega\right)=0. \end{cases} \tag{9}$$

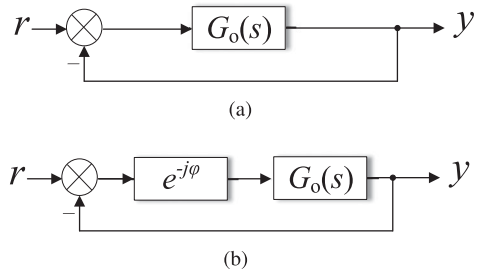

Fig. 5. Unit negative feedback system. (a) Without phase tester $e^{-j\varphi}$. (b) With phase tester $e^{-j\varphi}$.

By solving the expressions of K_{p} and K_{i} with respect to ω, it is shown as follows:

$$\begin{cases} K_{\mathrm{p}}=-\dfrac{a\left(\omega\right)}{a^2\left(\omega\right)+b^2\left(\omega\right)} \\ K_{\mathrm{i}}=-\dfrac{\omega b\left(\omega\right)}{a^2\left(\omega\right)+b^2\left(\omega\right)} \end{cases} \tag{10}$$

where $\omega\in(0,\infty)$, and the boundary of D-partition method consists of $a_0(k)=0, a_n(k)=0$, and (10).

In addition, by adding a phase tester $e^{-j\varphi}$ in Fig. 5(a), the D-partition boundary satisfying phase margin P_m can be flexibly obtained, as shown in Fig. 5(b). For example, if $\varphi=P_m$, the D-partition boundary satisfying P_m is obtained.

C. Stability Analysis of CSM-Controlled GCI Based on D-Partition Method

According to the principle of the D-partition method mentioned above, the stability region of CSM-controlled GCI meets desired multiperformance-index constraints can be obtained according to the following steps.

Step 1: Obtain the closed-loop characteristic equation of $G_{\mathrm{cl\_CSM}}(s)$, then calculate and plot the values of $K_{\mathrm{p\_CSM}}$ and $K_{\mathrm{i\_CSM}}$ in $K_{\mathrm{p\_CSM}}$-$K_{\mathrm{i\_CSM}}$ plane when ω changes from 0 to ∞. Finally, plot the curves corresponding to different bandwidth B_w of current-control loop in K_{pCSM}-K_{iCSM} plane.

It will obtain the stability region meeting the requirements of gain margin $G_m\geq 5$ dB, phase margin $30^\circ\leq P_m\leq 45^\circ$ and control bandwidth $500\,\mathrm{Hz}\leq B_w\leq 750\,\mathrm{Hz}$, as shown in the shaded area in Fig. 6. The PI gains selected in this shaded area will guarantee the dynamic and steady-state performance of the CSM-controlled GCI under the ideal grids without grid impedance. An arbitrary point on the curve, for example (217, 440 000) in Fig. 6, can be selected to plot the Bode diagram of the open-loop transfer function of the CSM-controlled GCI, as shown in Fig. 7. It can be found that the P_m and G_m are 3° and 5 dB, respectively, at this time, which is consistent with the results of the D-partition method shown in Fig. 6.

Step 2: Obtain stability boundaries under large SCR fluctuations. By selecting the PI parameter points in the shaded area, the requirements of multiple performance indexes mentioned above will be satisfied simultaneously. Moreover, the selected PI parameters will not be changed anymore and will then be used to analyze the stability of the GCI under different SCR. According to the impedance-based stability criterion [27], if

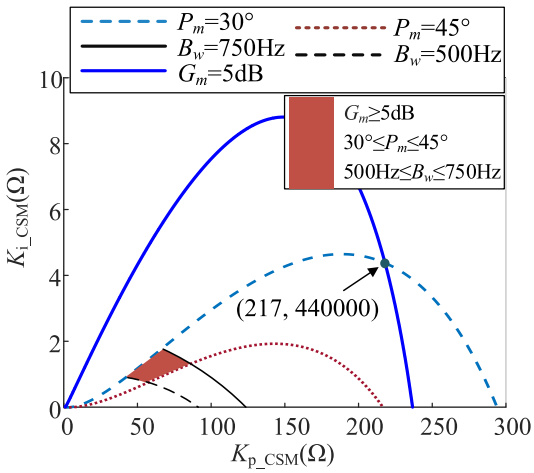

Fig. 6. Stability region of CSM-controlled GCI meeting the requirements of $G_m \geq 5$ dB, $30° \leq P_m \leq 45°$, and 500 Hz $\leq$ B_w $\leq$ 750 Hz based on the D-partition method.

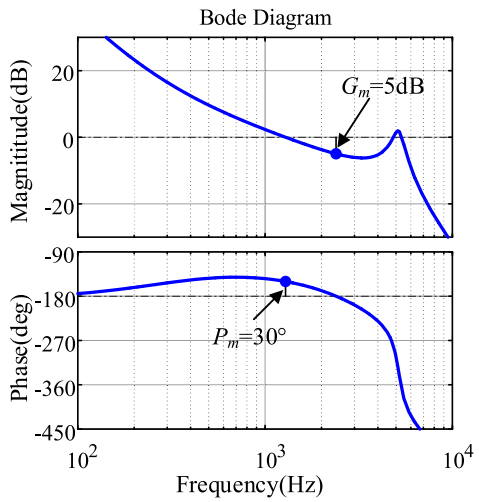

Fig. 7. Bode diagram of the open-loop transfer function with PI gains of (217, 440 000) in Fig. 6.

$sL_g/Z_{oCSM}(s)$ meets enough phase margin P_{mZo}, then the CSM-controlled GCI will be stable. It is worth mentioning that P_{mZo} represents the phase margin of the cascaded system of the CSM-controlled GCI tied to a weak grid with a certain grid impedance.

It will obtain the values of K_{p_CSM} and K_{i_CSM} in K_{p_CSM}-K_{i_CSM} plane under different SCRs when ω changes from 0 to ∞, as shown in Fig. 8. From Fig. 8, the decrease in SCR causes the curve of $P_{mZo} = 30°$ to gradually shrink and the area satisfying $P_{mZo} = 30°$ to become smaller. The 3-D graph of the curve of $P_m = 30°$ under large fluctuations of SCR is shown in Fig. 9. It is more clearly seen that these contour lines gradually shrink as the SCR decreases. Moreover, since ignoring negative-sequence impedance results in a nonconservative approach [29], Fig. 9 also shows the corresponding curves in the positive and negative sequences, and it can be seen that the area enclosed by the corresponding curves of the positive sequence is smaller than that of the negative sequence, which proves that the positive sequence system determines the stability of the GCI.

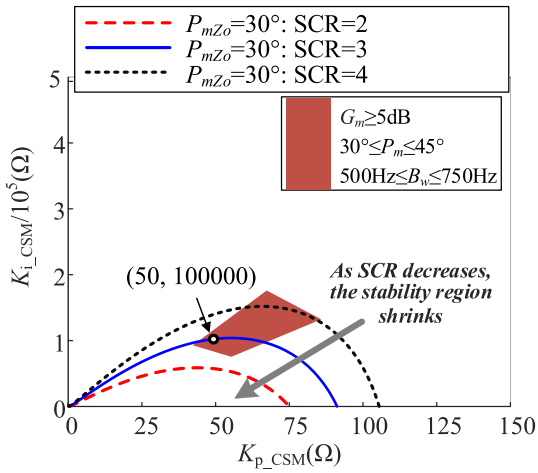

Fig. 8. Corresponding parameter stability region changes when SCR is 2, 3, and 4, respectively.

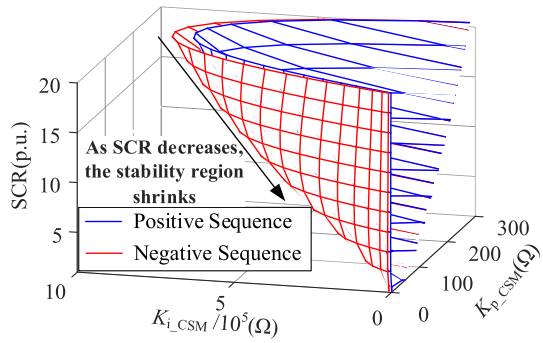

Fig. 9. Three-dimensional graph of the stability region of the CSM-controlled GCI as SCR changes from 1 to 20 based on the D-partition method.

In summary, if the PI gains of the CSM-controlled GCI are (50, 100 000) and $P_{mZo} = 30°$ under the weak grid, it can be seen from Fig. 8 that the D-partition curve just intersects (50, 100 000) when SCR=3. This indicates that SCR=3 is the critical stability boundary for the CSM-controlled GCI under the multiperformance-index constraints, i.e., $G_m \geq 5$ dB, $30° \leq P_m \leq 45°$, 500 Hz $\leq B_w \leq$ 750 Hz, and $P_{mZo} = 30°$.

D. Effect of PLL Bandwidth on the Stability of CSM-Controlled GCI

Fig. 10 shows the Bode diagram of $Z_{o\_VSM\_p}(s)$ with different PLL bandwidth ω_{PLL}. From Fig. 10, the phase margin $P_{mZo} = 30°$ for the CSM-controlled GCI when $\omega_{PLL} = 1$ p.u., which is consistent with the analytical results of the D-partition method in Fig. 8. The simulation model corresponding to Fig. 3 is built in MATLAB/Simulink and the output impedance characteristics are swept. The simulation results are shown in the dotted line in Fig. 10 when $\omega_{PLL} = 1$ p.u. The simulation results are in good agreement with the model results.

Moreover, the effect of PLL bandwidth ω_{PLL} on the above obtained stability boundary will be analyzed below. It can be seen from Fig. 10 that a high PLL bandwidth will cause $Z_{oCSM}(s)$ to be less than $-90°$ within 100 Hz, and P_{mZo} <0 at this time will directly cause additional low-frequency resonance

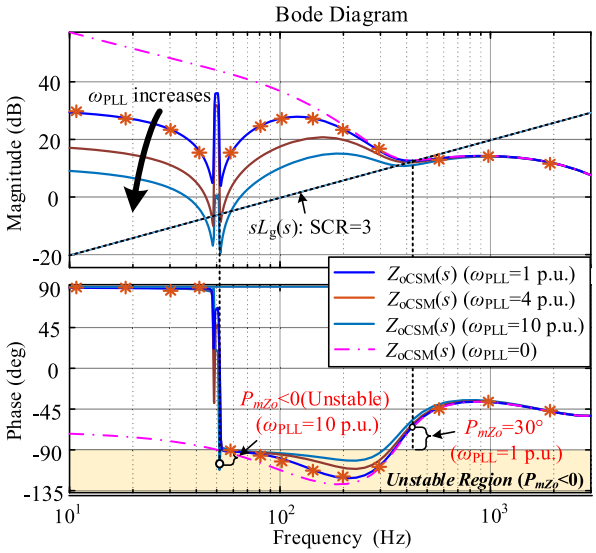

Fig. 10. Bode diagram of $Z_{o\_CSM\_p}(s)$ under different PLL bandwidth ω_{PLL}.

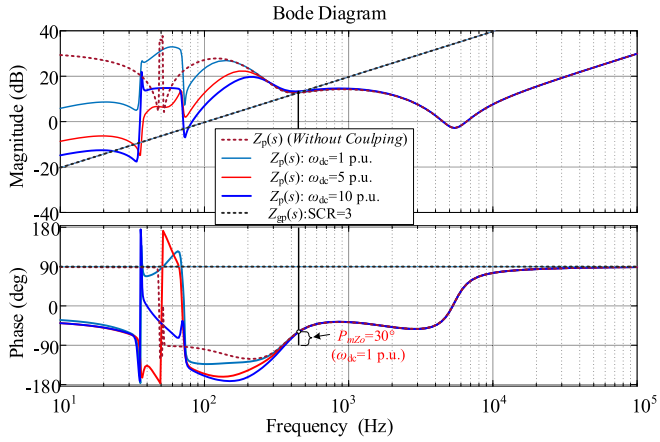

Fig. 11. Bode diagram of the equivalent output impedance at different bandwidths of the dc voltage loop when considering the frequency-coupling term.

within 100 Hz. This resonance is different from the middle and high frequency oscillations caused by the PI gains of the current loop. Therefore, once the effect of high PLL bandwidth is taken into account, in order to avoid low-frequency resonances up to 100 Hz, the SCR range of the GCI under CSM control must be appropriately increased, i.e., the stability boundary of SCR must be greater than 3. However, in practice, when the grid changes from strong to weak, the CSM-controlled GCI often adopts some improved control without switching to VSM directly, for example, adaptively adjusting the PLL bandwidth control to attenuate the effect of PLL [13]. Thus the stability boundary obtained from the previous analysis (i.e., SCR=3) is the maximum range over which the grid impedance of the CSM-controlled GCI can operate stably. Once SCR<3, even with improvement strategies such as reducing PLL bandwidth, the CSM-controlled GCI will not be able to meet the above constraints on multiple performance indexes and must switch to VSM control.

E. Effect of Frequency-Coupling Terms on the Stability of CSM-Controlled GCI

For the three-phase GCI after considering the frequency-coupling characteristics, a voltage excitation will not only produce a current response of the same frequency, but also a current response of other frequencies, i.e., the frequency-coupling phenomenon. This phenomenon has the characteristics of single input and multiple outputs (SIMO), the output positive sequence and negative sequence are no longer decoupled, and the traditional single-input–single-output (SISO) stability criterion is no longer applicable [30], [31]. In this case, the output impedance model will be a multi-input–multi-output (MIMO) system, as shown as follows:

$$Z_{o\_CSM}(s) = \begin{bmatrix} Z_{o\_CSM\_p}(s) & Z_{pn}(s-2j\omega_0) \\ Z_{np}(s) & Z_{o\_CSM\_n}(s-2j\omega_0) \end{bmatrix} \quad (11)$$

where the subdiagonal elements $Z_{pn}(s-2j\omega_0)$ and $Z_{np}(s)$ are the frequency-coupling terms.

Because of the existence of the frequency coupling, the stability analysis of the impedance model should usually use the generalized Nyquist criterion, but this method will not be able to determine the potential resonance points. Therefore, considering that the stability of a MIMO system is an inherent property of the system, independent of the number and value of its input and output signals, Vieto and Sun [30] reconstructs a MIMO system to several decoupled SISO systems, pointing out that the frequency-coupling terms can be regarded as an additional parallel impedance added to the output impedance impedance, and the stability can be determined using the traditional Nyquist criterion.

The detailed output impedance model of the CSM-controlled GCI is derived in [30], and it pointed out that in the lower frequency band, the frequency-coupling term and the impedance on the main diagonal are comparable in magnitude. Therefore, the effect of frequency-coupling effect is not negligible, and the degree of influence is related to the control bandwidth of the dc voltage loop. Fig. 11 shows the Bode diagram of the equivalent output impedance $Z_p(s)$ at different bandwidths of the dc voltage loop ω_{dc} when considering the frequency-coupling terms. From Fig. 11, the larger ω_{dc}, the greater the effect of frequency-coupling on the impedance of the low-frequency band, while it does not affect the impedance of middle and high frequency bands. When SCR=3 and ω_{dc}=1 p.u., the impedance effect of frequency-coupling on the low-frequency band does not intersect with the amplitude curve of the grid impedance, and the phase margin $P_{mZo} = 30°$, which is consistent with the analysis results when the frequency-coupling term is ignored in the Section II-C. The reason is the above obtained stability boundary of the CSM-controlled GCI is under the constraints of multiple performance indexes such as gain margin, phase margin and control bandwidth, which are directly related to the current-loop PI parameters of the CSM control. The bandwidth of the current loop is usually much larger than the control bandwidth of the dc voltage loop, so as long as the control bandwidth of the dc voltage loop is not too large (e.g., $\omega_{dc} \leq 1$

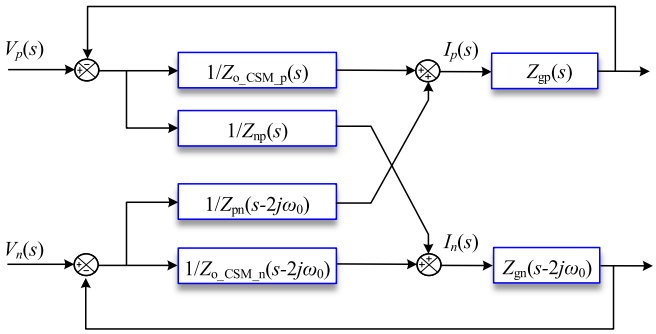

Fig. 12. Schematic diagram of the network structure of the impedance-coupling model.

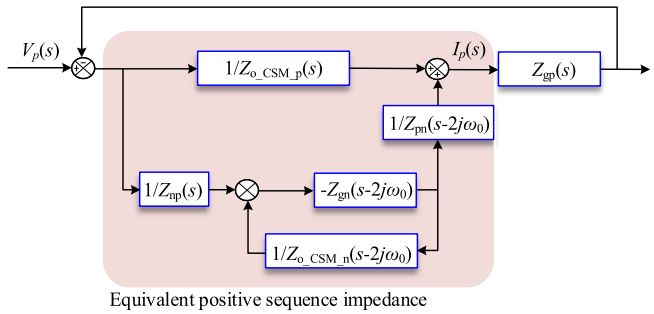

Fig. 13. Decoupled positive-sequence impedance model.

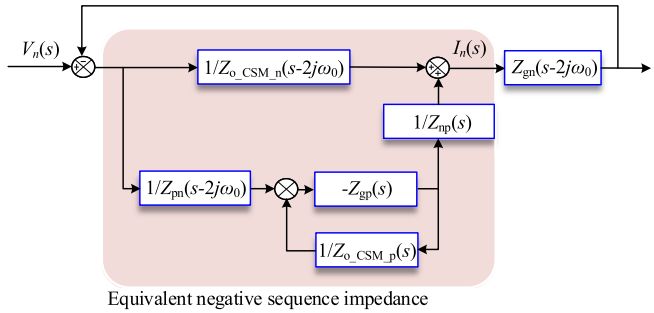

Fig. 14. Decoupled negative-sequence impedance model.

p.u.), the frequency-coupling term will not affect the validity of the analysis results in this article. Moreover, once a larger control bandwidth of the dc voltage loop is adopted, to avoid the low-frequency resonance due to the frequency coupling, the stability boundary of the CSM-controlled GCI obtained from the previous analysis in Section II-C also needs to be increased appropriately, i.e., the SCR must be greater than 3, and then the GCI must be switched from CSM control to VSM control. In addition, according to the conclusions in [30], the D-partition method can be applied to the MIMO system, and the reasons are described as follows:

From (11), the schematic diagram of the network structure of the impedance-coupling model can be obtained as shown in Fig. 12. A decomposition of the loops in Fig. 12 can transform this impedance-coupling model into the decoupled positive- and negative-sequence impedance models, respectively. As shown in Figs. 13 and 14, the equivalent positive-sequence impedance and negative-sequence impedance can be obtained. Therefore,

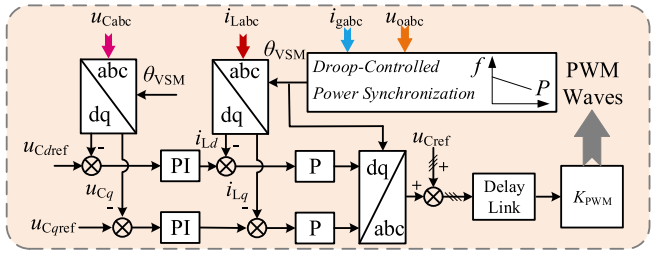

Fig. 15. Control structure of the VSM-controlled GCI.

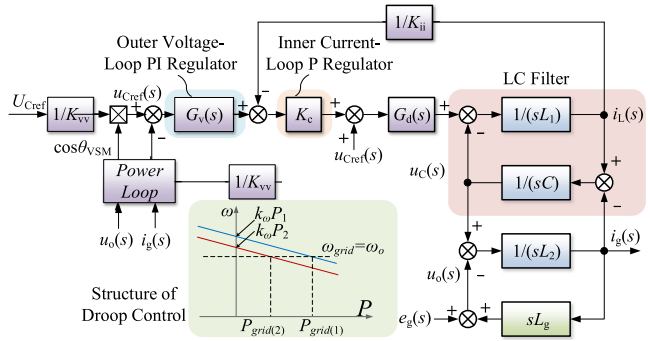

Fig. 16. Control block diagram of the VSM-controlled GCI.

the stability of the MIMO system (i.e., the impedance-coupling system) can be determined directly by the impedance-based stability criterion [27]. According to the implementation steps of the D-partition method introduced in the Section II-C, the expression between the controller parameters and the frequency ω will be obtained by solving the characteristic equation of the impedance-ratio transfer function. Finally, the stability boundaries as ω increases from 0 to ∞ will be plotted, and the area enclosed by these boundaries and the coordinate axes will be the stability region of the MIMO system.

III. Modeling and Stability Analysis of VSM-Controlled GCI Based on D-Partition Method

Similar to Section II, a mathematical model of the typical control topology of the VSM-controlled GCI in a weak grid will be constructed, and its stability boundary with the constraints of multiperformance index under large SCR fluctuations will be obtained based on the D-partition method.

A. Modeling of VSM-Controlled GCI

According to [6], [32], the control structure and control block diagram of the voltage-controlled GCI are illustrated in Figs. 15 and 16, respectively. In Fig. 15, the main circuit of the GCI is same as Fig. 2. u_{Cdref}, u_{Cqref} are the d-axis and q-axis components of the reference voltage u_{Cabcref} in the voltage loop. θ_{VSM} is the phase obtained by the droop-controlled power synchronization loop according to u_{oabc} and i_{gabc}, and the output power of the VSM-controlled GCI is changed by shifting the droop curve. From Fig. 16, the expression of the transfer function the output voltage is as follows:

$$u_{\mathrm{o}}(s) = G_{\mathrm{cl\_VSM}}(s)u_{\mathrm{Cref}}(s) - i_{\mathrm{g}}(s)Z_{\mathrm{o\_VSM}}(s) \qquad (12)$$

where $G_{\mathrm{cl\_VSM}}(s)$ and $Z_{\mathrm{o\_VSM}}(s)$ are the closed-loop transfer function and the output impedance of the VSM-controlled GCI, respectively. $G_{\mathrm{cl\_VSM}}(s)$ can be divided into positive-sequence closed-loop transfer function $G_{\mathrm{cl\_VSM\_p}}(s)$ and negative-sequence closed-loop transfer function $G_{\mathrm{cl\_VSM\_n}}(s)$, $Z_{\mathrm{o\_VSM}}(s)$ can be divided into positive-sequence impedance $Z_{\mathrm{o\_VSM\_p}}(s)$ and negative-sequence impedance $Z_{\mathrm{o\_VSM\_n}}(s)$. They are expressed as follows:

$$G_{\mathrm{cl\_VSM\_p}}(s)=\frac{G_{\mathrm{v}}(s-j\omega_0)K_{\mathrm{c}}G_{\mathrm{d}}(s)/K_{\mathrm{vv}}}{\left\{\begin{array}{l}s^2L_1C+sCK_{\mathrm{c}}G_{\mathrm{d}}(s)/K_{\mathrm{ii}}+1\\+G_{\mathrm{v}}(s-j\omega_0)K_{\mathrm{c}}G_{\mathrm{d}}(s)/K_{\mathrm{vv}}\end{array}\right\}} \tag{13}$$

$$G_{\mathrm{cl\_VSM\_n}}(s)=\frac{G_{\mathrm{v}}(s+j\omega_0)K_{\mathrm{c}}G_{\mathrm{d}}(s)/K_{\mathrm{vv}}}{\left\{\begin{array}{l}s^2L_1C+sCK_{\mathrm{c}}G_{\mathrm{d}}(s)/K_{\mathrm{ii}}+1\\+G_{\mathrm{v}}(s+j\omega_0)K_{\mathrm{c}}G_{\mathrm{d}}(s)/K_{\mathrm{vv}}\end{array}\right\}} \tag{14}$$

$$Z_{\mathrm{o\_VSM\_p}}(s)=sL_2+\frac{sL_1+K_{\mathrm{c}}G_{\mathrm{d}}(s)/K_{\mathrm{ii}}}{\left\{\begin{array}{l}s^2L_1C+sCK_{\mathrm{c}}G_{\mathrm{d}}(s)/K_{\mathrm{ii}}\\+G_{\mathrm{v}}(s-j\omega_0)K_{\mathrm{c}}G_{\mathrm{d}}(s)/K_{\mathrm{vv}}+1\end{array}\right\}} \tag{15}$$

$$Z_{\mathrm{o\_VSM\_n}}(s)=sL_2+\frac{sL_1+K_{\mathrm{c}}G_{\mathrm{d}}(s)/K_{\mathrm{ii}}}{\left\{\begin{array}{l}s^2L_1C+sCK_{\mathrm{c}}G_{\mathrm{d}}(s)/K_{\mathrm{ii}}\\+G_{\mathrm{v}}(s+j\omega_0)K_{\mathrm{c}}G_{\mathrm{d}}(s)/K_{\mathrm{vv}}+1\end{array}\right\}}. \tag{16}$$

In (13)–(16), K_{vv} is the sampling coefficient of the voltage sensor, K_{c} is the gain of inner current-loop proportional (P) regulator. $G_{\mathrm{v}}(s)=K_{\mathrm{p\_VSM}}+K_{\mathrm{i\_VSM}}/s$ represents the outer voltage-loop PI regulator.

B. Stability Analysis of VSM-Controlled GCI Based on D-Partition Method

Similar to CSM-controlled GCI, the stability region meeting the requirements of gain margin $G_m \geq 5$ dB, phase margin $30^\circ \leq P_m \leq 45^\circ$ and control bandwidth 2500 Hz $\leq B_w \leq$ 2550 Hz will be obtained, as shown in the shaded area in Fig. 17. It is worth mentioning that the VSM control shown in Fig. 16 uses direct voltage command feedforward control, which can effectively increase the control bandwidth of the voltage loop. An arbitrary point on the curve, for example (0.05, 3223) in Fig. 17, can be selected to plot the Bode diagram of the open-loop transfer function of the VSM-controlled GCI, as shown in Fig. 18. From the Bode plot, it can be found that the P_m and G_m are 30° and 5 dB, respectively, at this time, which is consistent with the results of the D-partition method shown in Fig. 17.

Different from the CSM-controlled GCI, it can be seen in Fig. 19 that the decrease in SCR causes the curve of $P_{mZo}=30^\circ$ to gradually expands and the area satisfying $P_{mZo}=30^\circ$ to become larger. The 3-D graph of the curve of $P_{mZo}=30^\circ$ under large fluctuations of SCR is shown in Fig. 20. It is more clearly seen that these contour lines gradually expand as the SCR decreases. Fig. 20 also shows the area enclosed by the corresponding curves of the positive sequence is smaller than that of the negative sequence, which also proves that the positive sequence system determines the stability of the GCI.

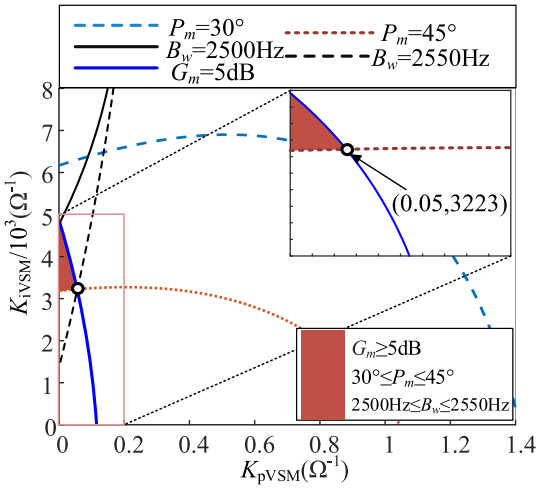

Fig. 17. Stability region of VSM-controlled GCI meeting the requirements of $G_m \geq 5$ dB, $30^\circ \leq P_m \leq 45^\circ$, and 2500 Hz $\leq B_w \leq$ 2550 Hz based on the D-partition method.

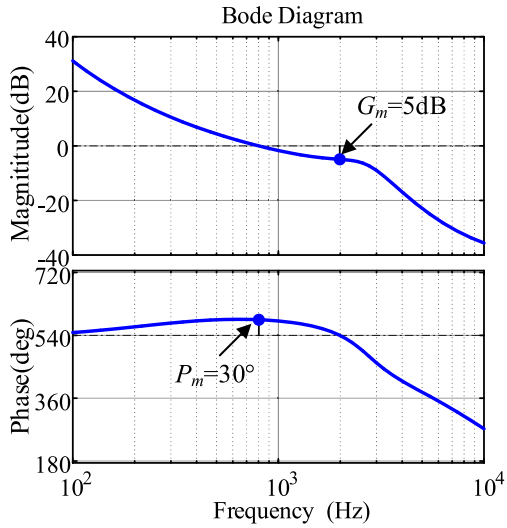

Fig. 18. Bode diagram of the open-loop transfer function with PI gains of (0.05, 3223) in Fig. 17.

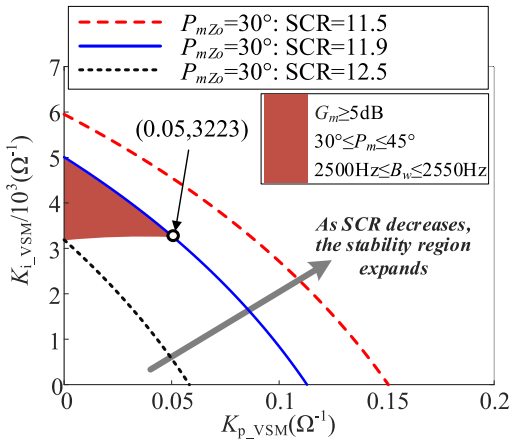

Fig. 19. Corresponding parameter stability region changes when SCR is 11.5, 11.9, and 12.5, respectively.

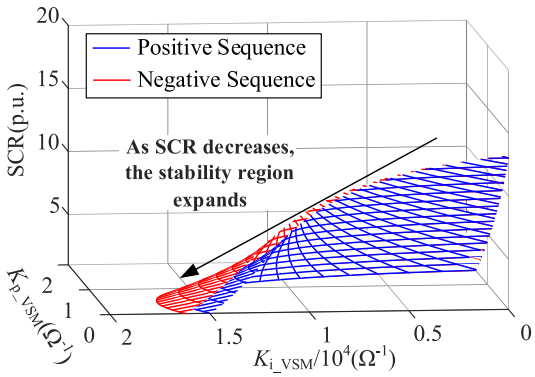

Fig. 20. Three-dimensional graph of the stability region of the VSM-controlled GCI as SCR changes from 1 to 20 based on the D-partition method.

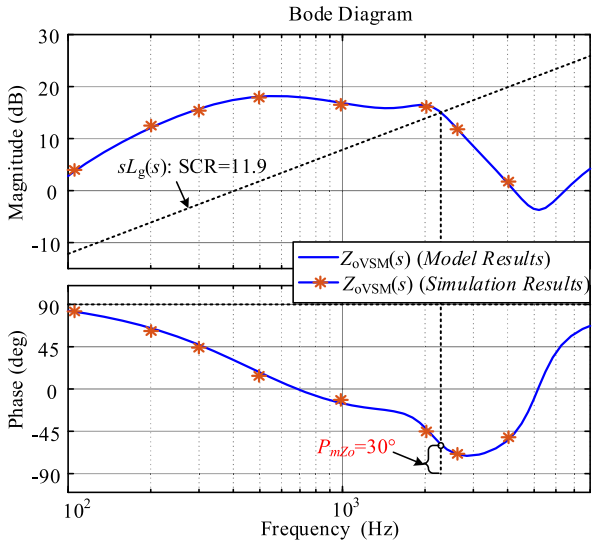

Fig. 21. Bode diagram of $Z_{o\_VSM\_p}(s)$ when PI gains are (0.05, 3223).

To verify the correctness of Fig. 19, when the PI gains are (0.05, 3223), the Bode diagram of $Z_{o\_VSM\_p}(s)$ is obtained as shown in Fig. 21. It can be seen that the amplitude curves of the output impedance and the grid impedance at SCR = 11.9 intersect in the middle and high frequency bands, corresponding to a phase margin of $P_{mZo} = 30°$, which is consistent with the analysis results of the D-partition method described above. The simulation model corresponding to Fig. 15 is built in MATLAB/Simulink and the output impedance characteristics are swept, and the results obtained are represented by the dotted lines in Fig. 21. The simulation results agree well with the results of the mathematical model, which verifies the correct modeling of the VSM-controlled GCI.

In summary, if the PI gains of the VSM-controlled GCI are (0.05, 3223) and $P_{mZo} = 30°$ under the weak grid, it can be seen from Fig. 19 that the D-partition curve just intersects (0.05, 3223) when SCR is 11.9. This indicates that SCR=11.9 is the critical stability boundary for the VSM-controlled GCI under the multiperformance-index constraints, i.e., $G_m \geq 5$ dB, $30° \leq P_m \leq 45°$, 2500 Hz $\leq B_w \leq$ 2550 Hz, and $P_{mZo} = 30°$.

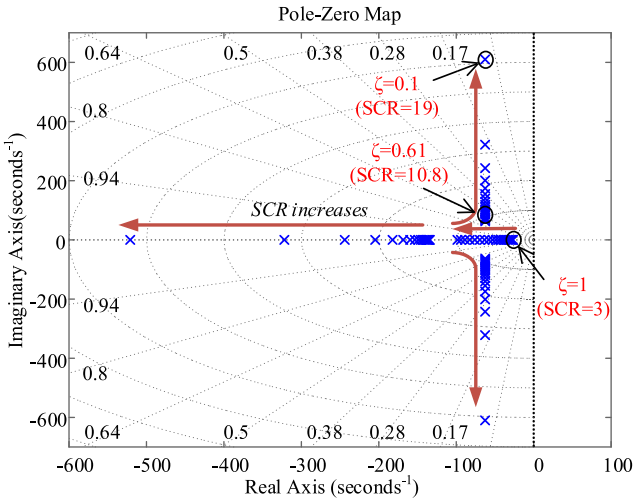

Fig. 22. Schematic diagram of poles of the droop-controlled power synchronization loop gradually moves away from the real-axis as SCR increases.

C. Effect of the Droop-Controlled Power Synchronization Loop on the Stability of VSM-Controlled GCI

Different from the CSM-controlled GCI, the VSM-controlled GCI uses a droop-controlled power self-synchronization loop to achieve synchronization with the grid voltage phase [6]. Moreover, an additional low-pass filter (LPF) with a lower cutoff frequency is usually required for the harmonic component of the instantaneous electromagnetic power in the power self-synchronization loop. This LPF weakens the dynamic response speed of the power synchronous loop, resulting in a large difference between the bandwidth of this power loop and the bandwidth of the voltage and current inner loop. In other words, when analyzing the stability boundary of GCI controlled by VSM, it can be considered that the power loop and the voltage and current inner loop are mutually decoupled: the influence of the power self-synchronization control on the stability boundary of the VSM-controlled GCI is in the low-frequency band, while the voltage and current inner loop is in the middle- and high-frequency band. Therefore, the ratio of the output impedance based on the voltage and current inner loop to the grid impedance determines the stability of the VSM-controlled GCI in the middle and high frequency bands, while the stability in the low-frequency band can be determined by establishing a small-signal model between the power loop and the grid impedance. According to [6], the trend of the poles of the closed-loop characteristic equation of the power loop with increasing SCR can be obtained as shown in Fig. 22. It shows that as the SCR increases, the poles gradually move away from the real axis and their damping ratio ζ gradually decreases. For example, when SCR=19, ζ is only 0.1. Due to the insufficient damping ratio, the VSM-controlled GCI will have power underdamped oscillations when the power is disturbed. And, if the current protection threshold is too small, overcurrent protection will occur easily. The experimental results in Fig. 37 will verify this conclusion.

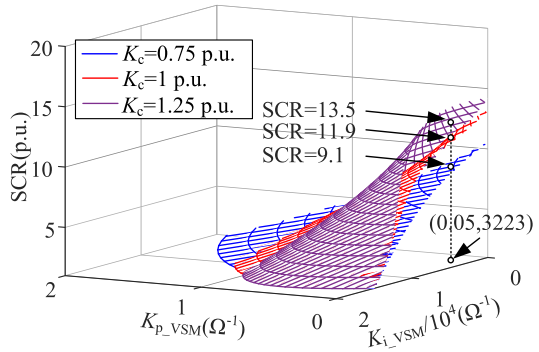

Fig. 23. Three-dimensional graph of the stability region of the VSM-controlled GCI as SCR changes from 1 to 20 based on the D-partition method for different K_c.

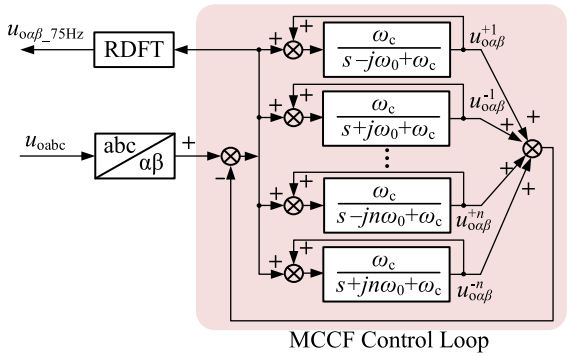

Fig. 24. Schematic diagram of fundamental-frequency gird impedance identification strategy based on MCCF combined with RDFT.

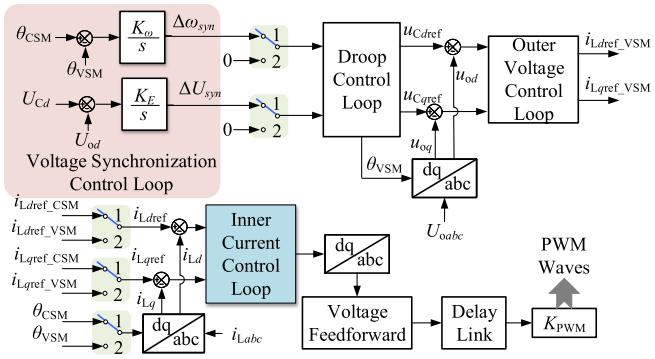

Fig. 25. Schematic diagram of the proposed dual-mode seamless switching scheme.

D. Effect of Inner Current-Loop Gain on the Stability of VSM-Controlled GCI

In the following, the effect of the inner current-loop gain K_c on the stability of the VSM-controlled GCI will be analyzed. The 3-D graph of the stability region of the VSM-controlled GCI as SCR changes from 1 to 20 based on the D-partition method for different K_c is shown in Fig. 23. As can be seen, the smaller the K_c, the smaller the stability boundary value obtained, for example, when K_c=1.25 p.u., the stability boundary value SCR=13.5 is obtained; when K_c=1 p.u., it drops to SCR=11.9; when K_c=0.75 p.u., it further drops to SCR=9.1.

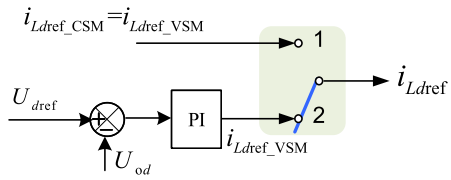

Fig. 26. Equivalent block diagram after GCI switching from CSM to VSM.

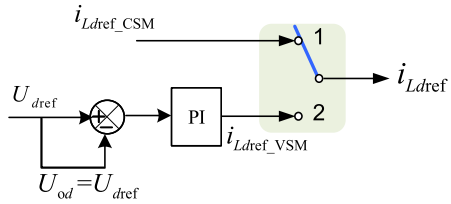

Fig. 27. Equivalent block diagram after GCI switching from VSM to CSM.

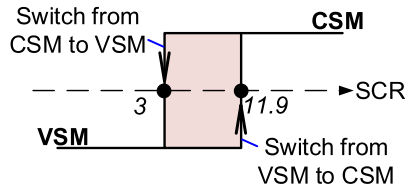

Fig. 28. Schematic diagram of CSM and VSM hysteresis switching process.

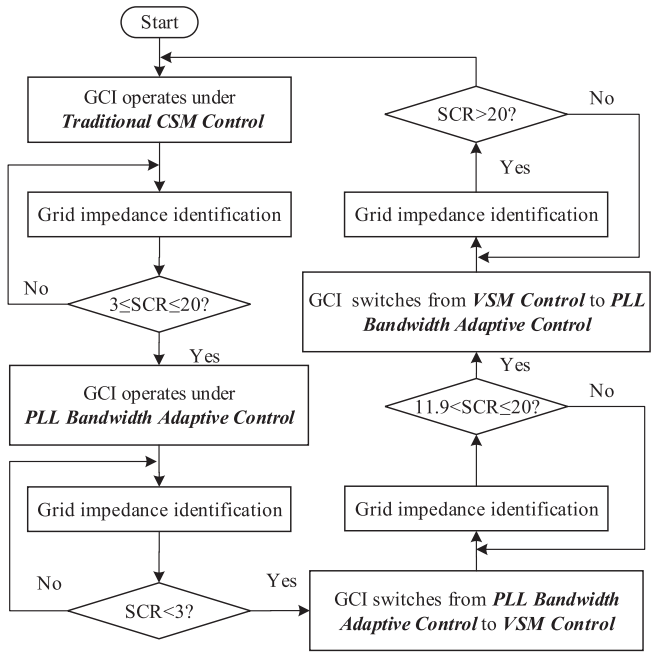

Fig. 29. Switching flowchart of impedance adaptive dual-mode control.

IV. Dual-Mode Seamless Switching Algorithm Based on Fundamental-Frequency Grid-Impedance Identification

A. Fundamental-Frequency Grid-Impedance Identification

According to [33], it is known that the grid impedance L_g at the fundamental frequency can be used to reflect the value of SCR. As the grid impedance at the fundamental frequency

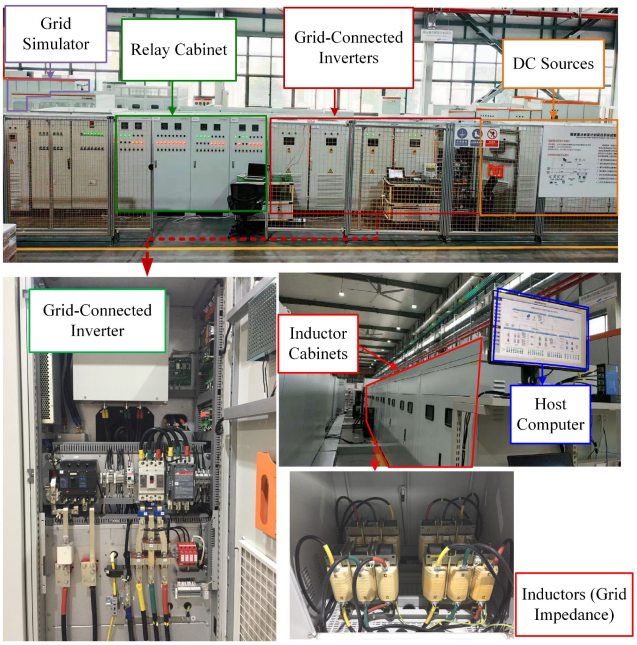

Fig. 30. Photograph of the 100-kW experimental platform.

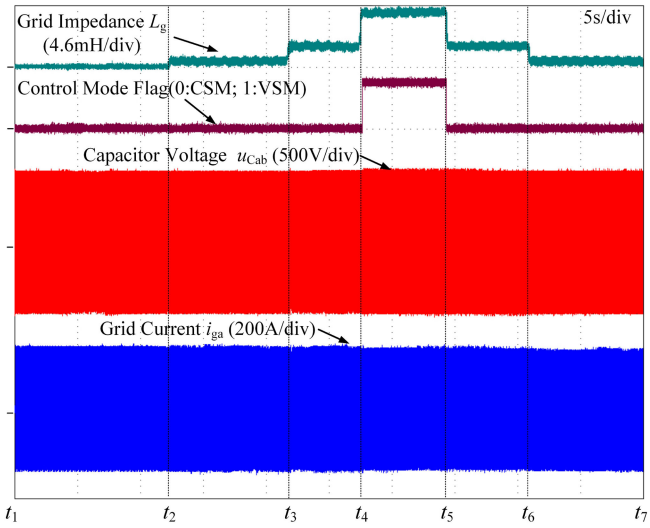

Fig. 31. Experimental waveforms of the dual-mode combined control strategy when SCR fluctuates greatly.

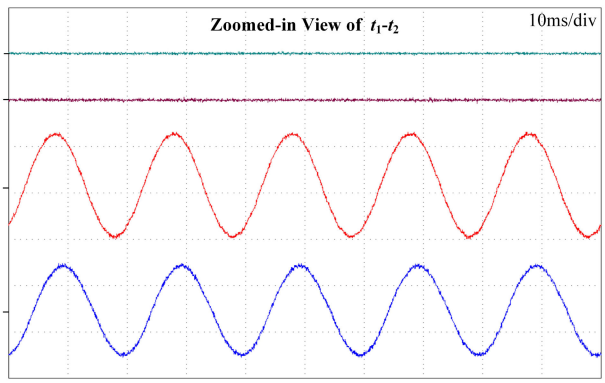

Fig. 32. Zoomed-in view of period $t_1 - t_2$ of the experimental waveforms shown in Fig. 31.

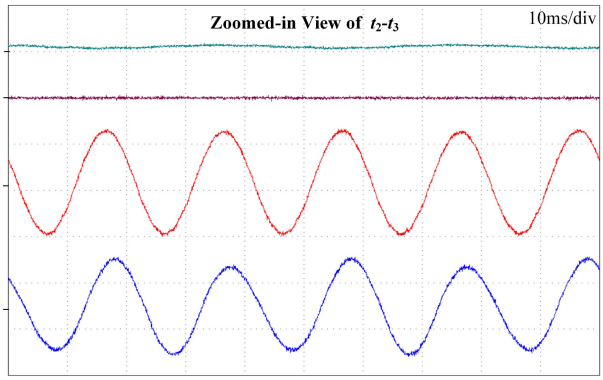

Fig. 33. Zoomed-in view of period $t_2 - t_3$ of the experimental waveforms shown in Fig. 31.

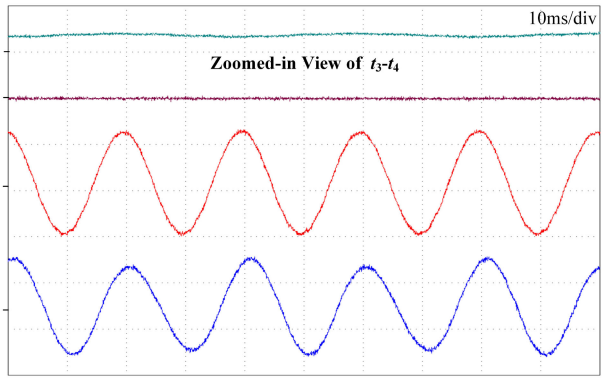

Fig. 34. Zoomed-in view of period $t_3 - t_4$ of the experimental waveforms shown in Fig. 31.

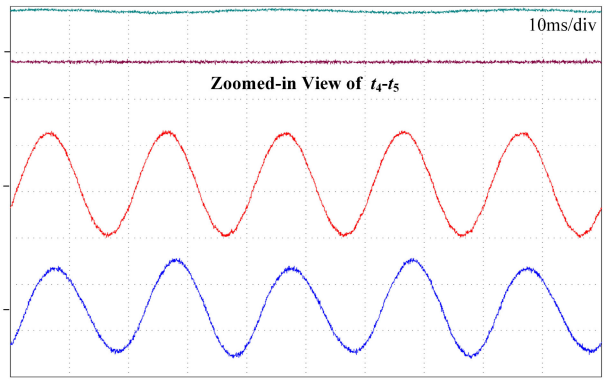

Fig. 35. Zoomed-in view of period $t_4 - t_5$ of the experimental waveforms shown in Fig. 31.

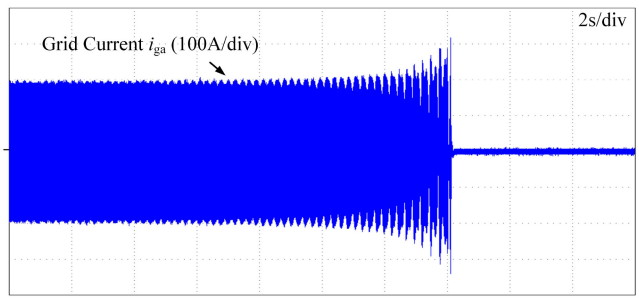

Fig. 36. Experimental waveform of GCI with traditional CSM control with high PLL bandwidth when SCR is reduced from 23 to 5.

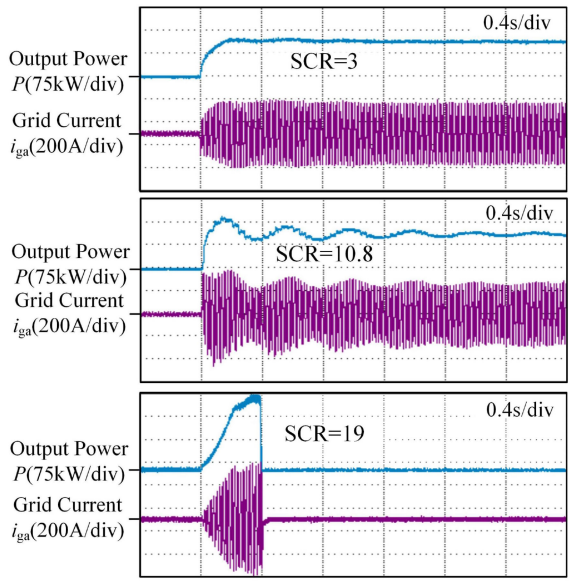

Fig. 37. Experimental waveforms of power step response damping of VSM-controlled GCIs under different SCR.

increases, the sensitivity of the voltage amplitude of the ac system to power variations will become more and more sensitive, and the corresponding SCR will be smaller [14]. Therefore, the fundamental-frequency grid impedance $Z_{g\mathrm{b}}(s)$ and its expression for the corresponding SCR can be defined as

$$Z_{g\mathrm{b}}(s)=sL_g\rho_1,\ \mathrm{SCR}=S_{sc}/S_1 \tag{17}$$

where S_{sc} is the short-circuit capacity of the ac grid, S_1 is the power generation capacity of the single GCI, and ρ_1 is the ratio of the power generation capacity of the single GCI to its rated capacity [33]. Therefore, the equivalent fundamental-frequency grid impedance from the perspective of the single GCI in a N multi-inverter system will be $Z_{g\_\mathrm{eq}}(s)=\sum_{i=1}^{N}(sL_g\rho_i)$, and the SCR of this multi-inverter system is

$$\mathrm{SCR}=\frac{Z_{g\mathrm{b}}(s)}{Z_{g\_\mathrm{eq}}(s)}\lambda_{\mathrm{bSCR}}=\frac{sL_g\rho_1}{\sum\limits_{i=1}^{N}(sL_g\rho_i)}\frac{S_{ac}}{S_1}. \tag{18}$$

For the method of identifying the grid impedance at the fundamental frequency, this article uses the steady-state technique of injecting an inter-harmonic voltage of 75 Hz at a frequency close to the fundamental frequency [34]. The response of the corresponding harmonic current and voltage to the grid impedance is measured by a novel algorithm proposed in this article, as shown in Fig. 24. Then, the CPU unit executes both CSM and VSM control algorithms and gives the grid impedance value.

The reason why interharmonic injection is used is as follows: since the existing harmonics on the grid do not coincide at the frequency of the interharmonic voltage injection, the effect is minimal, and it has the advantage of using a low signal level for the measurement.

The harmonic extraction method shown in Fig. 24 is described in detail: to eliminate the effects of the fundamental component of the grid voltage and multiple high-frequency background harmonics on the accuracy of the 75 Hz interharmonic voltage and current response, a scheme based on the multiple complex coefficient filters (MCCF) [35] combined with the recursive discrete Fourier transform (RDFT) [36] is proposed in this article, as shown in Fig. 24. The algorithm can ensure the processing speed of high-frequency harmonics through the MCCF control and achieve the suppression of the background harmonics of the grid voltage. While the RDFT updates the sampling in real time to ensure the identification accuracy and dynamic performance of the grid impedance at the fundamental frequency.

It is worth stating that obtaining grid impedance characteristics other than the fundamental frequency is undoubtedly useful for GCI control [37], but since the fundamental grid impedance determines the SCR, accurately determining the grid impedance over a wide frequency range will provide too much data than is actually needed. This determination of fundamental grid impedance does not require any special hardware, and the measurement process can be controlled, it is very convenient to determine the SCR values used in this article.

B. Dual-Mode Seamless Switching Scheme

In this article, a seamless dual-mode switching scheme between CSM and VSM is proposed, as shown in Fig. 25. The scheme takes into account that both modes have an internal current loop and can be switched without interference as long as the amplitude and phase of the current loop reference values are the same at the moment of mode switching. The specific process of switching implementation is as follows.

1) When all selector switches in Fig. 25 are switched from 1 to 2, GCI will switch from CSM to VSM.

a) Current Phase Synchronization: The VSM-controlled GCI adjusts its own output voltage amplitude U_{od} and phase θ_{VSM} through a presynchronization control link to track the amplitude and phase of the grid voltage in real time to achieve synchronization of the reference current phase between the CSM and VSM.

The expressions of the control algorithm for amplitude and phase synchronization are shown as follows:

$$\begin{cases}\Delta\omega_{syn}=(\theta_{\mathrm{CSM}}-\theta_{\mathrm{VSM}})\cdot K_\omega/s\\ \Delta U_{syn}=(U_{\mathrm{Cd}}-U_{\mathrm{od}})\cdot K_U/s\end{cases} \tag{19}$$

where $\Delta\omega_{syn}$ is the phase synchronization increment superimposed on the grid frequency ω_0, ΔU_{syn} is the amplitude synchronization increment superimposed on the grid voltage amplitude, and K_ω and K_U are the integral coefficients of the phase and amplitude synchronization control loop, respectively.

b) Current Amplitude Synchronization: Since there may be a difference between $i_{\mathrm{Ldref\_CSM}}$ and $i_{\mathrm{Ldref\_VSM}}$ at the moment of switching, in order to prevent sudden changes in the current command when switching from CSM to VSM, the GCI obtains the mode switching command by first using $i_{\mathrm{Ldref\_CSM}}$ and $i_{\mathrm{Ldref\_VSM}}$ as the initial and final values of the numerical slow starter, respectively, and after the adjustment of the numerical slow starter. The mathematical expression of this process is

$$i_{\mathrm{Ldref\_VSM}}=i_{\mathrm{Ldref\_CSM}}+\int_0^T\Delta i_{\mathrm{Ld}}dt \tag{20}$$

TABLE II
COMPARATIVE STABILITY OF CSM-CONTROLLED GCI AND VSM-CONTROLLED GCI

Control mode of the GCI		CSM	VSM
SCR range with different phase margin	$P_{mZo} \geq 30°$	$\mathrm{SCR} \geq 3$	$1 \leq \mathrm{SCR} \leq 11.9$
	$P_{mZo} \geq 45°$	$\mathrm{SCR} \geq 3.4$	$1 \leq \mathrm{SCR} \leq 9$
Variation trend of stability region under SCR variation		Stability region **shrinks** as SCR decreases	Stability region **expands** as SCR decreases
Influence of phase synchronization control on the stability of the GCI		High PLL bandwidth will cause the low-frequency resonance in weak grids	Droop-controlled power synchronization loop will cause the low-damping ratio in strong grids

where T is the slow start time from the initial value to the final value, Δi_{Ld} is the step size, and $\Delta i_{\mathrm{Ld}} = (i_{\mathrm{Ld\_ref\_VSM}} - i_{\mathrm{Ld\_ref\_CSM}})/T$. Make $i_{\mathrm{Ld\_ref\_CSM}}$ gradually change to $i_{\mathrm{Ld\_ref\_VSM}}$, then the slow start is over, at this time $i_{\mathrm{Ld\_ref\_CSM}}$=$i_{\mathrm{Ld\_ref\_VSM}}$, the switch will be switched from 1 to 2, to ensure smooth switching from CSM to VSM. The equivalent block diagram after switching from CSM to VSM is shown in Fig. 26.

2) When all selector switches are switched from 2 to 1, GCI will switch from VSM to CSM.

a) Current Phase Synchronization: The output voltage phase θ_{VSM} of GCI is clamped by the phase angle of the grid when GCI is under the VSM control, therefore, the phase in the process of switching from VSM to CSM is seamless.

b) Current Amplitude Synchronization: Compared with CSM control, VSM control has an extra voltage outer loop. In order to avoid the continuous integration of the voltage outer loop after VSM is switched to CSM, freeze the output of the voltage outer-loop PI regulator by setting the input of the voltage outer-loop PI regulator equal to 0, i.e., $U_{od} = U_{d\mathrm{ref}}$. At this time, the output of the voltage outer-loop PI regulator is kept as the value at the moment of mode switching, which is used as the current synchronization reference value when switching from CSM to VSM next time, thus avoiding the disturbance at the time of mode switching. The equivalent block diagram of PI regulator output latching after VSM switching to CSM is shown in Fig. 27.

C. Switching Flow Chart of Impedance Adaptive Dual-Mode Control

According to Sections II and III, the results shows the complementary stability region variation trend of the CSM-controlled GCI and VSM-controlled GCI under the SCR variation. In addition, by increasing the requirements of phase margin P_{mZo}, the stability range of the GCI under the control of these two modes will be decreased. Table II compares the stability of the GCIs in the two control modes in detail.

Based on the stability boundaries of the CSM and VSM shown in Table II, the mode switching process shown in Fig. 28 can be obtained. From Fig. 28, it is clear that the dual-mode switching process constitutes a hysteresis loop, which ensures that the CSM and VSM switching process will be jitter-free.

Fig. 29 shows the switching flow chart of impedance adaptive dual-mode control. The CSM-controlled GCI has the following two control cases.

1) *Traditional CSM control* refers to the absence of improved strategies such as active damping control, modified grid voltage feedforward control, and reduced PLL bandwidth, etc. This control strategy enables efficient and stable operation of GCI in strong grids.
2) *PLL bandwidth adaptive control* is an improved control of CSM. According to Fig. 10, the adaptive adjustment of PLL bandwidth is used to suppress the low-order resonance up to 100 Hz.

According to *IEEE Standard 1547-2003*, SCR>20 is often defined as a strong grid [38]. Therefore, the switching boundary for *traditional CSM control* and *PLL bandwidth adaptive control* is defined as SCR=20 in Fig. 29. It is worth mentioning that the choice of the actual mode switching boundary is more flexible and can often be conservative. For example, the critical boundary of CSM switching to VSM is set to SCR=3, which can ensure that the system has a phase margin of 30°, but the margin requirement can also be reduced appropriately, and the switching boundary can then be set to SCR=2 or even lower.

V. EXPERIMENTAL RESULTS

To verify the above analysis and the validity of the proposed method, an 100-kW experimental platform was established as shown in Fig. 30. The parameters of the GCI are listed in Table I. Different grid impedance values are realized by actual reactors in the grid impedance cabinet, and the removal and cut-in of these reactors are controlled by relays in the relay cabinet, thus simulating a large fluctuation scenario of the SCR.

A. Experimental Results of the Impedance Dual-Mode Control Strategy

Fig. 31 shows the experimental waveforms of the impedance adaptive dual-mode control strategy under large SCR fluctuations. It can be seen that the adaptive process includes a total of seven time points from t_1-t_7. The specific experimental process is described as follows.

1) t_1-t_2: The 0.2 mH inductor is put into the system at t_1, which makes the system SCR=23, thus simulating a strong grid situation. The GCI is operated at full power under traditional CSM control, during which the grid impedance identification algorithm is not enabled. The grid current i_{ga} and capacitor voltage u_{Cab} are running steadily, the grid impedance output value is 0, and the GCI operation mode flag is 0, indicating that the GCI is operating under CSM.

2) t_2-t_3: The grid impedance identification algorithm is enabled at t_2. Since SCR=23>20, the GCI remains in traditional CSM control according to the control mode flag in Fig. 31. It can be seen that after enabling the grid impedance identification algorithm, the corresponding SCR=23 is accurately obtained. Moreover, there is a 75 Hz harmonic response in the $i_{\rm ga}$ and $u_{\rm Cab}$ affected by the 75 Hz harmonics injected by the grid impedance identification algorithm.
3) t_3-t_4: Continue to put into 0.7 mH inductor at t_3, which reduces SCR from 23 to 5 and simulates weak grid scenario. According to Section III, since 3<SCR=5<20, the GCI operates under PLL bandwidth adaptive control. Similar time period t_2-t_3, the grid impedance algorithm is able to track the change of grid impedance in real time and obtain the SCR=5 at this time. Although the grid becomes weaker, the $i_{\rm ga}$ and $u_{\rm Cab}$ still operate stably because the PLL bandwidth of the CSM-controlled GCI can be reduced adaptively.
4) t_4-t_5: At t_4, the SCR is reduced from 5 to 2.6 by continuing to put into 1.1 mH inductor and simulating much weaker grid condition. Since SCR=2.6<3, the GCI switches from PLL bandwidth adaptive control to VSM. It can be seen that the grid impedance algorithm is still able to accurately identify the grid impedance and obtain the SCR=2.6 at this time. Similarly, although the grid becomes further weaker, the stability margin of the VSM-controlled GCI is still enough according to the previous analysis, so the $i_{\rm ga}$ and $u_{\rm Cab}$ can still operate stably.
5) t_5-t_6: Cut off 1.1 mH inductor at t_5, the experimental waveforms during this period are consistent with t_3-t_4.
6) t_6-t_7: Cut off 0.7mH inductor at t_6, the experimental waveforms during this period are consistent with t_2-t_3.

Figs. 32–35 show the zoomed-in view of t_1-t_2, t_2-t_3, t_3-t_4, and t_4-t_5 and in Fig. 31, respectively. It can be seen that $i_{\rm ga}$ and $u_{\rm Cab}$ are operating stably during these period. Therefore, the experimental waveforms in Fig. 31 are fully consistent with the flow chart shown in Fig. 29, verifying the effectiveness of the proposed impedance adaptive dual-mode control during large SCR fluctuations.

As a comparative experimental verification of the effectiveness of the proposed control strategy, Fig. 36 shows the experimental waveform without the impedance adaptive dual-mode control strategy. In Fig. 36, the GCI is running in the traditional CSM control with high PLL bandwidth, and the SCR is reduced from 23 to 5. The $i_{\rm ga}$ undergoes low-frequency oscillations within 100 Hz and gradually diverges until overcurrent protection. According to Fig. 10, it can be seen that the phase margin of the GCI within 100 Hz is less than 0 with high PLL bandwidth, and the system will be unstable at this time. This experimental result verifies the conclusion.

B. Experimental Results of the Effect of the Droop-Controlled Power Synchronization Loop on the Stability of VSM-Controlled GCI

Fig. 37 shows the waveforms when the output active power command of the VSM controlled-GCI steps from 0 to the rated value when the SCR is 3, 10.8, and 19, respectively. It can be seen that the overshoot of the output active power gradually increases as the SCR gradually decreases, indicating that the damping ratio of the power loop is decreasing, which is consistent with the analysis results in Fig. 22. If the SCR is too large, for example, when SCR=19, the GCI will be shut down due to overcurrent protection. This experimental result verifies that the VSM-controlled GCI will be unstable in a strong grid.

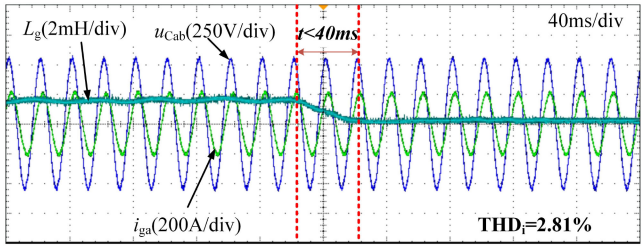

Fig. 38. Experimental waveforms of the proposed fundamental-frequency grid-impedance identification.

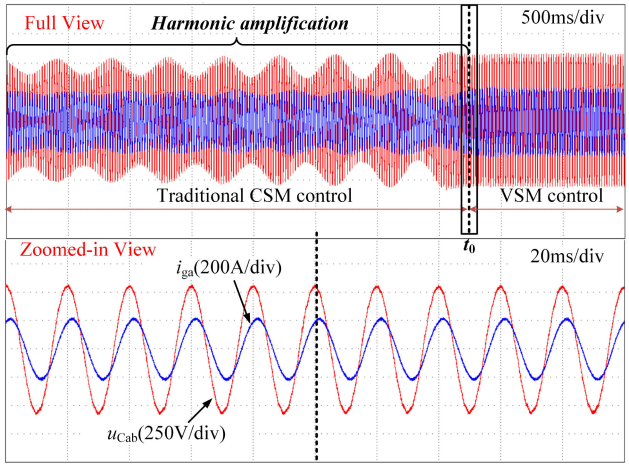

Fig. 39. Experimental waveforms of the dual-mode seamless switching scheme.

C. Experimental Results of the Proposed Fundamental Frequency Grid Impedance Identification

The experimental waveforms of the proposed fundamental frequency grid impedance identification is shown in Fig. 38. It can be seen that the algorithm accurately tracks the changes of the fundamental frequency grid impedance and the dynamic process time is less than 40 ms. In addition, the total harmonic distortion (THD) of the grid current is about 2.81% after injecting the 75 Hz interharmonic voltage with an amplitude of 5% of the rated voltage. Therefore, the proposed grid impedance identification scheme has a small impact on the control performance of GCI and meets the requirements of relevant grid-connected quality standards.

D. Experimental Results of the Proposed Dual-Mode Seamless Switching Scheme

Fig. 39 shows the experimental waveforms of the proposed dual-mode seamless switching. The switching principle

is shown in Fig. 25. The specific experimental progress are described as follows. The SCR of the grid is set to 2.6. Before t_0, the GCI operates under the traditional CSM control, and the i_{ga} and u_{Cab} show significant low-order harmonic amplification. At t_0, the GCI is switched from CSM to VSM by the command sent from the host computer, at which time the harmonic amplification disappears. This verifies that VSM control is more stable in very weak grids than CSM control. Moreover, it can be seen from the zoomed-in view of the experimental waveforms that the phase and amplitude of the grid current are switched seamlessly at t_0. Similarly, the experimental waveforms for seamless switching from VSM to CSM is also similar.

VI. Conclusion

Based on the D-partition method, the stabilization region of impedance adaptive dual-mode control under multiperformance-index constraints is derived, and the switching boundary problem of the dual-mode control is solved. In addition, the real-time fluctuation of SCR is accurately detected by the proposed grid impedance identification algorithm on the 100-kW experimental platform, and the flexible adaptive seamless switching between CSM and VSM is realized, which effectively improves the stability of GCI when the SCR fluctuates significantly.

It is also worth mentioning that only the parameter stability region of single GCI under dual-mode control is analyzed, and the multi-GCI systems should be considered in future work. Once extended to a power electronics-based multi-inverter system, the grid impedance may consist of inductors and converters, and its stability analysis will be more complicated. This is one of the main research aspects of the proposed dual-mode control strategy in the future.

References

[1] M. Liserre, R. Teodorescu, and F. Blaabjerg, "Stability of photovoltaic and wind turbine grid-connected inverters for a large set of grid impedance values," *IEEE Trans. Power Electron.*, vol. 21, no. 1, pp. 263–272, Jan. 2006.

[2] D. Zhu, S. Zhou, X. Zou, and Y. Kang, "Improved design of PLL controller for LCL-type grid-connected converter in weak grid," *IEEE Trans. Power Electron.*, vol. 35, no. 5, pp. 4715–4727, May 2019.

[3] W. Rui, S. Qiuye, M. Dazhong, and H. Xuguang, "Line impedance cooperative stability region identification method for grid-tied inverters under weak grids," *IEEE Trans. Smart Grid*, vol. 11, no. 4, pp. 2856–2866, Jul. 2020.

[4] W. Wu, Y. Liu, Y. He, H. S.-H. Chung, M. Liserre, and F. Blaabjerg, "Damping methods for resonances caused by LCL-filter-based current-controlled grid-tied power inverters: An overview," *IEEE Trans. Ind. Electron.*, vol. 64, no. 9, pp. 7402–7413, Sep. 2017.

[5] X. Chen, X. Ruan, D. Yang, W. Zhao, and L. Jia, "Injected grid current quality improvement for a voltage-controlled grid-connected inverter," *IEEE Trans. Power Electron.*, vol. 33, no. 2, pp. 1247–1258, Feb. 2017.

[6] M. Li, X. Zhang, Y. Yang, and P. Cao, "The grid impedance adaptation dual mode control strategy in weak grid," in *Proc. IEEE Int. Power Electron. Conf.*, 2018, pp. 2973–2979.

[7] S.-K. Chung, "A phase tracking system for three phase utility interface inverters," *IEEE Trans. Power Electron.*, vol. 15, no. 3, pp. 431–438, May 2000.

[8] M. P. Kazmierkowski and L. Malesani, "Current control techniques for three-phase voltage-source PWM converters: A survey," *IEEE Trans. Ind. Electron.*, vol. 45, no. 5, pp. 691–703, Oct. 1998.

[9] S. Silwal, S. Taghizadeh, M. Karimi-Ghartemani, M. J. Hossain, and M. Davari, "An enhanced control system for single-phase inverters interfaced with weak and distorted grids," *IEEE Trans. Power Electron.*, vol. 34, no. 12, pp. 12 538–12551, Dec. 2019.

[10] D. Dong, B. Wen, D. Boroyevich, P. Mattavelli, and Y. Xue, "Analysis of phase-locked loop low-frequency stability in three-phase grid-connected power converters considering impedance interactions," *IEEE Trans. Ind. Electron.*, vol. 62, no. 1, pp. 310–321, Jan. 2014.

[11] X. Cao, G. Liu, W. Xu, and W. Wang, "Adaptive quasi-PRD control method of grid-connected PV inverter under weak grid," in *Proc. IEEE 9th Int. Conf. on Power Electron. ECCE Asia*, 2015, pp. 2469–2474.

[12] J. Xu, S. Xie, and T. Tang, "Improved control strategy with grid-voltage feedforward for LCL-filter-based inverter connected to weak grid," *IET Power Electron.*, vol. 7, no. 10, pp. 2660–2671, Oct. 2014.

[13] M. Cespedes, *Impedance Modeling, Analysis, and Adaptation of Grid-Connected Inverters With PLL*. Troy, NY, USA: Rensselaer Polytechnic Institute, 2014.

[14] L. Zhang, L. Harnefors, and H.-P. Nee, "Interconnection of two very weak AC systems by VSC-HVDC links using power-synchronization control," *IEEE Trans. Power Syst.*, vol. 26, no. 1, pp. 344–355, Feb. 2010.

[15] X. Yuan, F. Wang, D. Boroyevich, Y. Li, and R. Burgos, "DC-link voltage control of a full power converter for wind generator operating in weak-grid systems," *IEEE Trans. Power Electron.*, vol. 24, no. 9, pp. 2178–2192, Sep. 2009.

[16] W. Wu *et al.*, "Sequence impedance modeling and stability comparative analysis of voltage-controlled VSGs and current-controlled VSGs," *IEEE Trans. Ind. Electron.*, vol. 66, no. 8, pp. 6460–6472, Aug. 2019.

[17] R. Lanzkron and T. Higgins, "D-decomposition analysis of automatic control systems," *IRE Trans. Autom. Control*, vol. 4, no. 3, pp. 150–171, Dec. 1959.

[18] Y. I. Neimark, "Robust stability and d-partition," *Autom. Remote Control*, vol. 53, no. 7, pp. 957–965, 1992.

[19] A. Shenton and Z. Shafiei, "Relative stability for control systems with adjustable parameters," *J Guid. Control Dyn.*, vol. 17, no. 2, pp. 304–310, Mar. 1994.

[20] Z. Shafiei and A. Shenton, "Tuning of PID-type controllers for stable and unstable systems with time delay," *Automatica*, vol. 30, no. 10, pp. 1609–1615, Oct. 1994.

[21] H. Li, X. Zhang, S. Yang, F. Li, J. Yang, and P. Cao, "Analysis and design of IPMSM drive system based on visualization technique in discrete time domain," in *Proc. IEEE Energy Convers. Congr. Expo.*, 2017, pp. 1940–1946.

[22] H. Li *et al.*, "Multi-objective visual analysis of PI current regulator for high performance PMSM drives," in *Proc. IEEE 8th Int. Power Electron. Motion Control Conf.*, 2016, pp. 1368–1372.

[23] E. Twining and D. G. Holmes, "Grid current regulation of a three-phase voltage source inverter with an LCL input filter," *IEEE Trans. Power Electron.*, vol. 18, no. 3, pp. 888–895, May 2003.

[24] F. Liu, Y. Zhou, S. Duan, J. Yin, B. Liu, and F. Liu, "Parameter design of a two-current-loop controller used in a grid-connected inverter system with LCL filter," *IEEE Trans. Ind. Electron.*, vol. 56, no. 11, pp. 4483–4491, Nov. 2009.

[25] P. Hušek, "Decentralized PI controller design based on phase margin specifications," *IEEE Trans. Control Syst. Technol.*, vol. 22, no. 1, pp. 346–351, Jan. 2013.

[26] J. Sun, Z. Bing, and K. J. Karimi, "Input impedance modeling of multipulse rectifiers by harmonic linearization," *IEEE Trans. Power Electron.*, vol. 24, no. 12, pp. 2812–2820, Dec. 2009.

[27] J. Sun, "Impedance-based stability criterion for grid-connected inverters," *IEEE Trans. Power Electron.*, vol. 26, no. 11, pp. 3075–3078, Nov. 2011.

[28] X. Chen, Y. Zhang, S. Wang, J. Chen, and C. Gong, "Impedance-phased dynamic control method for grid-connected inverters in a weak grid," *IEEE Trans. Power Electron.*, vol. 32, no. 1, pp. 274–283, Jan. 2016.

[29] M. Beza and M. Bongiorno, "Identification of resonance interactions in offshore-wind farms connected to the main grid by MMC-based HVDC system," *Int. J. Elect. Power Energy Syst.*, vol. 111, pp. 101–113, Oct. 2019.

[30] I. Vieto and J. Sun, "Sequence impedance modeling and converter-grid resonance analysis considering DC bus dynamics and mirrored harmonics," in *Proc. IEEE 19th Workshop Control Model. Power Electron.*, 2018, pp. 1–8.

[31] S. Song, Z. Wei, Y. Lin, B. Liu, and H. Liu, "Impedance modeling and stability analysis of PV grid-connected inverter systems considering frequency coupling," *CSEE J. Power Energy Syst.*, vol. 6, no. 2, pp. 279–290, Jun. 2020.

[32] M. Li, X. Zhang, and W. Zhao, "A novel stability improvement strategy for a multi-inverter system in a weak grid utilizing dual-mode control," *Energies*, vol. 11, no. 8, Aug. 2018, Art. no. 2144.
[33] P. Krishayya *et al.*, IEEE Guide for Planning DC Links Terminating at AC Locations Having Low Short-Circuit Capacities, Part I: AC/DC System Interaction Phenomena," CIGRE, Paris, France, 1997, pp. 1–216.
[34] L. Asiminoaei, R. Teodorescu, F. Blaabjerg, and U. Borup, "A digital controlled PV-inverter with grid impedance estimation for ENS detection," *IEEE Trans. Power Electron.*, vol. 20, no. 6, pp. 1480–1490, Nov. 2005.
[35] Y. Terriche, S. Golestan, J. M. Guerrero, and J. C. Vasquez, "Multiple-complex coefficient-filter-based PLL for improving the performance of shunt active power filter under adverse grid conditions," in *Proc. IEEE Power Energy Soc. Gen. Meeting*, 2018, pp. 1–5.
[36] B. P. McGrath, D. G. Holmes, and J. J. H. Galloway, "Power converter line synchronization using a discrete fourier transform (DFT) based on a variable sample rate," *IEEE Trans. Power Electron.*, vol. 20, no. 4, pp. 877–884, Jul. 2005.
[37] M. Liserre, R. Teodorescu, and F. Blaabjerg, "*Stability of grid-connected PV inverters with large grid impedance variation*," in *Proc. IEEE 35th Annu. Power Electron. Specialists Conf.*, 2004, pp. 4773–4779.
[38] IEEE Standard for Interconnecting Distributed Resources With Electric Power Systems, IEEE Standard 1547-2003, 2003.

Ming Li (Member, IEEE) was born in Anhui, China, in 1993. He received the B.S. degree in electric engineering and automation and the Ph.D. degree in electric engineering from the Hefei University of Technology, Hefei, China, in 2014 and 2020, respectively.

His current research interests include control of photovoltaic converters, microgrid system, distributed generation systems, and stability analysis of grid-connected inverters.

Xing Zhang (Senior Member, IEEE) was born in Shanghai, China, in 1963. He received the B.S., M.S., and Ph.D. degrees in electrical engineering and automation from the Hefei University of Technology, Hefei, China, in 1984, 1990, and 2003, respectively.

Since 1984, he has been a Faculty Member with the School of Electric Engineering and Automation, Hefei University of Technology, where he is currently a Professor. He is also with the Photovoltaic Engineering Research Center of the Ministry of Education. His main research interests include photovoltaic generation technologies, wind power generation technologies, and distributed generation systems.

Zixuan Guo (Student Member, IEEE) was born in Hebei, China, in 1992. He received the B.S. degree in 2016 from the Hefei University of Technology, Hefei, China, where he is currently working toward the Ph.D. degree.

His current research interests includes the virtual synchronous generator (VSG) control strategy, stability analysis of grid-connected inverters, and photovoltaic generation technologies.

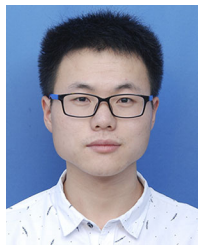

Hailong Pan was born in Anhui, China, in 1996. He received the B.S. degree in 2018 from the Hefei University of Technology, Hefei, China, where he is currently working toward the M.S. degree.

His current research interests include stability analysis of new energy grid-connected system, grid state estimation, and impedance identification algorithm.

Mingyao Ma (Member, IEEE) received the B.Sc. and Ph.D. degrees in applied power electronics and electrical engineering from Zhejiang University, Hangzhou, China, in 2004 and 2010, respectively.

Since 2015, she has been working with the Hefei University of Technology, Hefei, China, as a Professor. Her research interests include intelligent fault diagnosis of power electronic converter, health monitoring of power device, and intelligent operation and maintenance technology of photovoltaic power system.

Wei Zhao was born in Beijing, China, in 1973. He received the Ph.D. degree from the Hefei University of Technology, Hefei, China, in 2003.

He is currently a Senior Vice President with Sungrow Power Supply Company, Ltd., Hefei, China. His main research interests include photovoltaic generation technologies, distributed generation systems, and wind power generation technologies.